An Iterative Linear Method with Variable Shear Stress Magnitudes for Estimating the Stress Tensor from Earthquake Focal Mechanism Data: Method and Examples

Eric Beauce[1], Michel Campillo[1,1,1], Robert D Van Der Hilst[1,1,1], and Eric Beauce[1,2]

[1]Massachusetts Institute of Technology
[2]Columbia University

December 1, 2022

Abstract

Earthquake focal mechanism data provide information about the stress state at the origin of these earthquakes. The inversion methods that are commonly used to infer the stress tensor from focal mechanisms have varying complexity but always rely on a number of assumptions. We present an iterative method built upon a classic linear stress tensor inversion that allows to relax the assumption on shear stress magnitudes while preserving the computational simplicity of the linear problem. Every iteration of our method computes the least-squares solution of the problem, which makes the method fast enough to estimate the inverted parameter errors with non-parametric resampling methods such as bootstrapping. Following previous studies, this method removes the fault plane ambiguity in focal mechanism data by selecting the nodal plane that best satisfies the Mohr-Coulomb failure criterion. We first test the performance and the robustness to noise of the proposed method on synthetic data sets, and then apply it to data from Southern California and from the Geysers geothermal field. We focus the study on investigating the consequences of relaxing the assumption of constant shear stress magnitudes. Our variable shear method successfully generalizes its constant shear counterpart: it is able to perform similarly when the constant shear assumption is a good approximation and provides more accurate results when it is not. We provide the Python package ILSI to implement the proposed method.

An Iterative Linear Method with Variable Shear Stress Magnitudes for Estimating the Stress Tensor from Earthquake Focal Mechanism Data: Method and Examples

Eric Beaucé[a,c], Robert D. van der Hilst[a], Michel Campillo[b,a]

[a] *Department of Earth, Atmospheric, and Planetary Sciences, Massachusetts Institute of Technology, Cambridge, MA, United States*
[b] *Institut des Sciences de la Terre, Université Grenoble Alpes, Grenoble, France*
[c] *Lamont-Doherty Earth Observatory, Columbia University, NY, United States*

Abstract

Earthquake focal mechanism data provide information about the stress state at the origin of these earthquakes. The inversion methods that are commonly used to infer the stress tensor from focal mechanisms have varying complexity but always rely on a number of assumptions. We present an iterative method built upon a classic linear stress tensor inversion that allows to relax the assumption on shear stress magnitudes while preserving the computational simplicity of the linear problem. Every iteration of our method computes the least-squares solution of the problem, which makes the method fast enough to estimate the inverted parameter errors with non-parametric resampling methods such as bootstrapping. Following previous studies, this method removes the fault plane ambiguity in focal mechanism data by selecting the nodal plane that best satisfies the Mohr-Coulomb failure criterion. We first test the performance and the robustness to noise of the proposed method on synthetic data sets, and then apply it to data from Southern California and from the Geysers geothermal field. We focus the study on investigating the consequences of relaxing the assumption of constant shear stress magnitudes. Our variable shear method successfully generalizes its constant shear counterpart: it is able to perform similarly when the constant shear assumption is a good approximation and provides

more accurate results when it is not. We provide the Python package ILSI to implement the proposed method.

Corresponding Author:

Eric Beaucé, ebeauce@ldeo.columbia.edu

Lamont-Doherty Earth Observatory

Columbia University

61 Route 9W, 220 Seismology

Palisades, NY 10964

USA

Declaration of Competing Interests.

The authors acknowledge there are no conflicts of interest recorded.

1. Introduction

The sense of motion on faults carries information on the stress state surrounding these faults. Field measurements of fault orientations and slip directions (slickensides) were first used to retrieve the stress tensor using a number of assumptions [*e.g.* Carey et al., 1974; Angelier, 1979; Angelier et al., 1982]. The cornerstone assumption of these methods is that slickensides are oriented along the direction of maximum shear stress resolved on the faults [the so-called Wallace-Bott assumption, Wallace, 1951; Bott, 1959]. Stress tensor inversion techniques were extended to the more widely available earthquake focal mechanism data, which describe faulting from seismic observations instead of direct field measurements. In general, the inverse problem is non-linear and solving it requires grid-search or other global optimization methods [Angelier et al., 1982; Gephart and Forsyth, 1984], but

with additional assumptions the problem can be linearized [*e.g.* Michael, 1984]. Both non-linear and linear inversion techniques suffer from the ambiguity in earthquake focal mechanism data that provide two possible fault planes per datum, without offering the possibility to identify the actual fault plane [the consequences of choosing the wrong plane are discussed at length in Michael, 1987b]. While some of the non-linear inversion methods choose the fault planes as the set of planes that minimize their objective function [such as the algorithm implemented in Focal Mechanism Stress Inversion, FMSI, Gephart, 1990], other criteria, physics-based and independent from the objective function, are preferred to avoid data over-fitting. Lund and Slunga [1999] introduced the use of the Mohr-Coulomb failure criterion to select fault planes.

In this work, we present an inversion method built upon the linearized problem due to Michael [1984], turning it into an iterative inversion while preserving the computational efficiency of the least-squares solution of a linear problem. We thus relax the assumption made by Michael [1984] that shear stress magnitude is constant across faults or, equivalently, that all faults are optimally oriented within the stress field. Following previous studies [Lund and Slunga, 1999; Vavryčuk, 2014], we also use the Mohr-Coulomb failure criterion to select fault planes. The proposed method is implemented by our Python package ILSI (Iterative Linear Stress Inversion, see Data and Resources). The scope of this study is to demonstrate the efficacy of our method to effectively solve the non-linear problem involving variable shear stress magnitudes, and that it performs similarly or better than its constant shear counterpart [namely, the method proposed in Vavryčuk, 2014] on realistic data sets and under challenging noise conditions, while eliminating one assumption about the data.

2. Methodology

2.1. Previous Work

Given a fault plane with orientation described by its unitary normal $\hat{n}$, the traction on the plane is:

$$T = \sigma\hat{n}, \tag{1}$$

where σ is the Cauchy stress tensor, and T is the traction. The normal T_n and tangential (shear) T_t components of the traction are:

$$\begin{aligned} T_n &= (\sigma\hat{n}\cdot\hat{n})\hat{n} = \sigma_n\hat{n} \\ T_t &= T - T_n = \sigma\hat{n} - (\sigma\hat{n}\cdot\hat{n})\hat{n} = \tau\hat{t}. \end{aligned} \tag{2}$$

In Equation (2), σ_n and τ are the magnitudes of the normal and shear tractions, respectively. The direction of shear traction is given by the unit vector $\hat{t}$. The stress tensor is often represented by its eigendecomposition: the principal stress directions $\hat{\sigma}_i$ (eigenvectors) and the principal stresses σ_i (eigenvalues, $i = 1, 2, 3$). A plane that is perpendicular to $\hat{\sigma}_i$ does not experience any shear, and is under a purely compressional traction of magnitude σ_i. By convention, eigenvalues are ordered such that σ_1 is the most compressional stress, σ_3 is the least compressional stress and σ_2 is the intermediate stress. Note that in terms of deviatoric stresses (the stress minus the lithostatic pressure), σ_1 is the compression axis and σ_3 is the extension axis.

Stress tensor inversion of earthquake focal mechanism data commonly relies on two assumptions:

- the stress tensor is homogeneous in space,

- slip on faults occur in the direction of maximum resolved shear stress [Wallace-Bott assumption, Wallace, 1951; Bott, 1959].

An earthquake focal mechanism is a descriptor of the orientation and slip direction of a fault, based on the radiation pattern of seismic waves. Because of the symmetry of radiation patterns, there exists two fault planes with different slip directions that describe the same focal mechanism. The fault normal $\hat{n}$ and slip direction $\hat{s}$ of a given fault plane can be interchanged to describe slip on an auxiliary plane that produces the same radiation pattern. Thus, each focal mechanism datum provides two possible fault normals $\hat{n}$ and slip directions $\hat{s}$. We describe later a way of solving this ambiguity, but will assume for now that the fault plane and slip direction are known. Based on the Wallace-Bott assumption, one seeks the stress tensor that predicts shear directions $\hat{t}$ that best match the slip directions $\hat{s}$. This inverse problem does not provide any information on the absolute stress magnitudes, therefore it can only retrieve the reduced stress tensor, *i.e.* a normalized deviatoric stress tensor σ^*:

$$\mathrm{Tr}(\sigma^*) = \sum_{k=1}^{3} \sigma^*_{kk} = 0; \qquad \sum_{i,j} (\sigma^*_{ij})^2 = 1. \tag{3}$$

For simplicity, hereinafter we keep using σ instead of σ^*. One can only obtain four independent parameters from the inverse problem: the three principal stress directions $\hat{\sigma}_i$, and the shape ratio R,

$$R = \frac{\sigma_1 - \sigma_2}{\sigma_1 - \sigma_3}. \tag{4}$$

This scalar quantity is a measure of the relative magnitude of the principal stresses. In terms of deviatoric stress, if $R > 0.5$, σ_2 is extensional, and conversely if $R < 0.5$ then σ_2 is compressional. One can think of R as describing the position of σ_2 in between σ_1 and σ_3 on the x-axis of a Mohr circle (see Figure 1).

For a population of faults described by their normals $\hat{n}_i$ and their slip directions $\hat{s}_i$, writing Equation (2) for each fault and identifying the shear direction $\hat{t}_i$ to the slip direction $\hat{s}_i$ yields the following system of equations for shear tractions:

$$\sigma\hat{n}_i - (\sigma\hat{n}_i \cdot \hat{n}_i)\hat{n}_i = \tau_i\hat{s}_i. \tag{5}$$

The inverse problem consists of finding σ such that Equation (5) is satisfied on each fault i. Unfortunately, even though the left-hand side of Equation (5) is linear in σ, the right-hand side is not because of the shear magnitude τ_i. Although one cannot determine the absolute shear magnitudes, the relative magnitudes between faults still matter. Several strategies have been proposed to solve the inverse problem: for example, Angelier et al. [1982] solve the non-linear problem iteratively, and the broadly used method due to Gephart and Forsyth [1984] adopts a grid-search over the four independent parameters to minimize their angular misfit (*i.e.* their objective function does not depend on shear magnitudes). These two methods consider errors not only in the slip directions but also in the orientation of the fault normals. The other widely used method is due to Michael [1984], which stands out by its simplicity, and which many other methods are built upon [for example, Hardebeck and Michael, 2006; Martínez-Garzón et al., 2014; Vavryčuk, 2014]. The author made the assumption that shear stress is relatively constant from fault to fault, thus assigning the shear magnitude on the right-hand side of Equation (5) a scalar (equal to one). While this assumption can be seen as a weakness of the method, it has also been argued that this is a physically reasonable assumption that regularizes the inversion [Michael, 1984]. We discuss the regularizing effect when analyzing our synthetic tests (Section 3). The linear problem is:

$$Gm = d \quad (6)$$

$$\underbrace{\begin{pmatrix} & & & & \\ & & & & \\ \hat{n}_{i,1} + \hat{n}_{i,1}\hat{n}_{i,3}^2 - \hat{n}_{i,1}^3 & \hat{n}_{i,2} - 2\hat{n}_{i,2}\hat{n}_{i,1}^2 & \hat{n}_{i,3} - 2\hat{n}_{i,3}\hat{n}_{i,1}^2 & \hat{n}_{i,1}\hat{n}_{i,3}^2 - \hat{n}_{i,1}\hat{n}_{i,2}^2 & -2\hat{n}_{i,1}\hat{n}_{i,2}\hat{n}_{i,3} \\ \hat{n}_{i,2}\hat{n}_{i,3}^2 - \hat{n}_{i,2}\hat{n}_{i,1}^2 & \hat{n}_{i,1} - 2\hat{n}_{i,1}\hat{n}_{i,2}^2 & -2\hat{n}_{i,1}\hat{n}_{i,2}\hat{n}_{i,3} & \hat{n}_{i,2} + \hat{n}_{i,2}\hat{n}_{i,3}^2 - \hat{n}_{i,2}^3 & \hat{n}_{i,3} - 2\hat{n}_{i,3}\hat{n}_{i,2}^2 \\ \hat{n}_{i,3}^3 - \hat{n}_{i,3} - \hat{n}_{i,3}\hat{n}_{i,1}^2 & -2\hat{n}_{i,1}\hat{n}_{i,2}\hat{n}_{i,3} & \hat{n}_{i,1} - 2\hat{n}_{i,1}\hat{n}_{i,3}^2 & \hat{n}_{i,3}^3 - \hat{n}_{i,3} - \hat{n}_{i,3}\hat{n}_{i,2}^2 & \hat{n}_{i,2} - 2\hat{n}_{i,2}\hat{n}_{i,3}^2 \\ & & & & \\ & & & & \end{pmatrix}}_{G} \underbrace{\begin{pmatrix} \sigma_{11} \\ \sigma_{12} \\ \sigma_{13} \\ \sigma_{22} \\ \sigma_{23} \end{pmatrix}}_{m} = \underbrace{\begin{pmatrix} . \\ . \\ \hat{s}_{i,1} \\ \hat{s}_{i,2} \\ \hat{s}_{i,3} \\ . \\ . \end{pmatrix}}_{d}$$

In Equation (6), d is the stack of all slip vectors and G is the stack of all matrices relating the stress tensor elements to the direction of shear stress on the faults. Given that we can only retrieve the deviatoric stress tensor (see Equation (3)), the last diagonal term that does not appear in Equation (6) is implicitly defined by $\sigma_{33} = -\sigma_{11} - \sigma_{22}$. The linear inverse problem defined by Equation (6) is usually solved in the least-squares sense, for example with the Tarantola and Valette formula [Tarantola and Valette, 1982]:

$$m = m_{\text{prior}} + \left(G^T C_D^{-1} G + C_M^{-1}\right)^{-1} G^T C_D^{-1} \left(d - G m_{\text{prior}}\right). \quad (7)$$

In Equation (7), m_{prior} is an approximate solution known a priori, C_D and C_M are the covariance matrices modeling the prior knowledge on the data and model parameter distributions, respectively. If no prior knowledge on the target solution is available, then $C_M^{-1} = 0$ and $m_{\text{prior}} = 0$. Note that

this linear formulation only considers errors in slip directions and not in fault orientations.

2.2. This Study

We relax the assumption of constant shear stress magnitudes in Michael [1984] by iteratively solving for both the stress tensor elements and the shear stress magnitudes. The algorithm is:

1. Initialize the solution:

$$m^{(0)} = \left(G^T C_D^{-1} G + C_M^{-1}\right)^{-1} G^T C_D^{-1} d^{(0)} \tag{8}$$

2. Compute shear stress magnitudes at iteration t and update the set of linear equations (*i.e.* update the estimate of the right-hand side of Equation (5)):

$$\tau_i^{(t)} = |\sigma^{(t)}\hat{n}_i - (\sigma^{(t)}\hat{n}_i \cdot \hat{n}_i)\hat{n}_i|; \qquad d_i^{(t)} = \tau_i^{(t)} d_i^{(0)} \tag{9}$$

3. Solve the updated linear inverse problem and update the stress tensor elements $m^{(t)}$ using the previous estimate $m^{(t-1)}$ as prior knowledge:

$$m^{(t)} = m^{(t-1)} + \left(G^T C_D^{-1} G + C_M^{-1}\right)^{-1} G^T C_D^{-1} \left(d^{(t)} - G m^{(t-1)}\right). \tag{10}$$

4. Repeat 2 and 3 until $|\tau^{(t)} - \tau^{(t-1)}|$ is lower than a user-provided threshold.

The superscript in parenthesis is the iteration index, the subscript i is the fault index, $d^{(0)}$ are the unitary slip vectors and C_M^{-1} is generally set to zero. C_D^{-1} can be used to give more or less weight to the observations based on their quality, or is equal to identity if all focal mechanisms are equally accurate. We emphasize that the shear stress magnitudes $\tau_i^{(t)}$ are not free parameters of the inversion, but are functions of the inverted stress tensor, and therefore do not promote data overfitting. In

Section 3, we show with synthetic examples that this iterative procedure produces similar robustness to data perturbation as the regular linear method of Michael [1984] and helps find more accurate solutions. In this study, we use the outward footwall normals and the slip direction of the hanging walls with respect to the footwalls, implicitly setting our stress tensor sign convention to *negative compression*. The formula relating strike/dip/rake to normal and slip vectors can be found, for example, in Chapter 4.2 of Stein and Wysession [2009].

When dealing with earthquake focal mechanism data sets, one needs to determine the fault planes out of the pairs of nodal planes in order to get an accurate estimate of the stress tensor [Michael, 1987b, illustrates how choosing the wrong planes impacts the solution]. We use the Mohr-Coulomb failure criterion to assess which planes are more likely to be the fault planes for a given stress tensor [Lund and Slunga, 1999]. We recall that this criterion states that a rupture occurs if the shear stress exceeds a critical value given by:

$$\tau_c = C + \mu\sigma_n, \tag{11}$$

where C and μ are the cohesion and the friction on the fault, respectively. We denote the effective normal stress on the fault by σ_n, meaning that we include any pore pressure in this term. The closer the shear stress τ is to the critical value, the more unstable the fault is. Therefore, a measure of fault instability is:

$$\Delta\tau = \tau - \tau_c = \tau - C - \mu\sigma_n = \tau - \mu(\sigma_n + C/\mu) = \tau - \mu\sigma_n^*. \tag{12}$$

In Equation (12), $\Delta\tau$ is the instability parameter as defined in Lund and Slunga [1999]. In Equations (11) and (12), σ_n is assumed to be positive in compression to retrieve Lund and Slunga [1999]'s

expression. Note that we included cohesion into the normal stress magnitude ($\sigma_n \rightarrow \sigma_n^*$). Since we do not have access to absolute values of stress, the cohesion is not a relevant variable in this analysis. This also means that $\Delta\tau$ as defined here only has a meaning in a relative sense, when comparing different planes. Therefore, following Vavryčuk et al. [2013], Vavryčuk [2014], we express normal stresses with respect to the maximum compression stress σ_1, and normalize the instability parameter by its value at the most unstable plane. The modified instability parameter I is defined as:

$$I = \frac{\tau - \mu(\sigma_1 - \sigma)}{\tau_c - \mu(\sigma_1 - \sigma_c)}. \tag{13}$$

This formula was derived assuming *negative compression* (that is $\sigma_1 < \sigma_2 < \sigma_3$) for consistency with the first part of the method. τ_c and σ_c are the shear stress and normal stress magnitudes of the most unstable fault. The different terms of Equation (13) are defined graphically in Figure 1. Note that, in Section 3, we will refer to the coefficient of friction in Equation (13) as μ_A ("μ algorithm"). Given a stress tensor σ, the fault plane that is chosen is the one that maximizes I out of the two nodal planes.

Finally, the inversion includes the following steps:

1. Initial guess of σ by randomly selecting sets of nodal planes.
2. Choose the fault planes based on I.
3. Inner loop: Iteratively run the linear inversion (Equations (8)-(10)).
4. Repeat 2 and 3 until convergence or a user-defined maximum number of iterations.

Ten iterations are usually sufficient to reach convergence. Our proposed method differs from the method described in Vavryčuk [2014] only by the addition of the inner loop (step 3) that solves the non-linear problem with variable shear stress magnitudes. Therefore, we refer to the method in

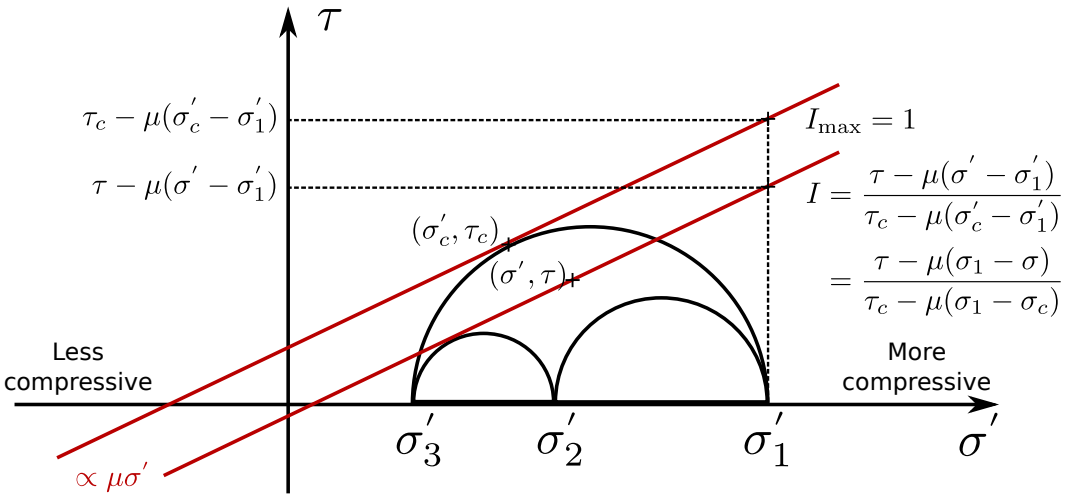

Figure 1: Definition of the instability parameter [Equation (13), following Vavryčuk et al., 2013] in the Mohr space where σ' is normal stress in the *positive compression* convention. The instability parameter in Equation (13) is written in terms of normal stress σ in the negative compression convention. The red straight lines are the failure lines whose slopes are controlled by the friction μ. The most unstable fault has coordinates (σ_c', τ_c') in the Mohr space. The σ_i''s are the principal stresses ordered from most compressive to least compressive.

Vavryčuk [2014] as the constant shear counterpart of our method. In the following, we sometimes loosely refer to the constant (variable) shear stress magnitudes method as the constant (variable) shear method.

Even though adding these iterations to the linear inversion from Michael [1984] makes our algorithm slower, it is still fast enough to be run many times on bootstrapped data sets to infer the parameter confidence intervals [Efron and Tibshirani, 1986]. Earlier studies have shown that bootstrap resampling in stress inversions infers more correct confidence intervals than methods using statistical hypotheses [*e.g.* Michael, 1987a; Hardebeck and Hauksson, 2001]. We use this non-parametric method to estimate uncertainties in the applications described in the next sections.

We note that using the Mohr-Coulomb failure criterion to select fault planes and iteratively solve for the stress tensor does not ensure convergence. Indeed, this is a feature of both our method and the methods described in Lund and Slunga [1999] and Vavryčuk [2014]. Problematic data sets may lead to an oscillatory solution. Given the stress tensor $\tau^{(t)}$ at iteration t, the selected set of nodal planes $\mathcal{S}^{(t)}$ depends on the outcome of the instability criterion $I(\tau^{(t)})$. Inverting this set of nodal planes produces a new stress tensor $\tau^{(t+1)}$ that, in turn, selects a new set of nodal planes $\mathcal{S}^{(t+1)}$. For example, a non-optimally oriented fault present in $\mathcal{S}^{(t)}$ may have a more unstable auxiliary plane that will be selected in $\mathcal{S}^{(t+1)}$. The inversion of $\mathcal{S}^{(t+1)}$ may yield a solution where the true fault plane is again more unstable, *et cetera*. The discrete nature of $\mathcal{S}$ implies that any change in the selected nodal planes translates into a sharp change in the associated fault normals. Because shear stress is a smooth function of the fault normal (Equation (2)), it also implies a sharp change in the inverted stress tensor. Despite oscillations of the solution in these problematic cases, one can still use this iterative procedure to explore different possible populations of faults, and select in the end the stress tensor that produces the lowest residuals. Ten iterations are, again, usually sufficient to explore the candidate solutions and select the best one. We suggest that the non-convergence of the algorithm indicates the inadequacy of a simple Mohr-Coulomb failure criterion, with a single coefficient of friction for all faults, to describe the real failure criterion. Non-converging instances reflect inherent uncertainties that can be estimated with the bootstrap resampling method.

3. Synthetic Experiments

The scope of this study is to demonstrate that relaxing the assumption of constant shear stress magnitudes is not detrimental to the robustness of the method with respect to its constant shear

counterpart [Vavryčuk, 2014], and also produce more accurate results. Because the equations of the forward and inverse problems (Equations (6) and (7)) remain the same in any orthonormal basis, the choice of the directions of principal stresses in the synthetic tests does not matter. However, the accuracy of the results is sensitive to the shape ratio. In order to simulate realistic data, focal mechanisms are synthesized such that they follow the Mohr-Coulomb failure criterion assuming some coefficient of friction. However, to avoid limiting the experiments to a simplistic failure criterion that would fit too well the method's assumptions, we investigate multiple data synthesis strategies such as randomly distributed coefficients of friction, or accepting with low probability focal mechanisms that do not satisfy the failure criterion (see full descriptions in Table 1). In order to restrict the synthetic earthquakes to physically plausible ruptures, we choose the cohesion parameter in the Mohr-Coulomb criterion such that the instability (Equation (13)) of the least unstable fault is $I_{\min} = 0.80$, *i.e.* the least unstable fault is 20% less unstable than the most unstable fault (the optimally oriented fault). To synthesize a focal mechanism, we randomly draw a fault plane orientation from a uniform distribution of strike and dip angles, and accept it if it satisfies the selection criterion (*e.g.* the Mohr-Coulomb criterion). Furthermore, because sampling uniformly the space of fault orientations does not produce a uniform distribution in the Mohr space, and does not even ensure that faults with higher instability are preferred (see Figure 2a), we accept valid fault planes with a probability that is proportional to instability ($p = (I - I_{\min})/(1 - I_{\min})$). This high instability preferential sampling produces more realistic data sets (*cf.* Figure 2b). We emphasize that, because of this sampling strategy, the lowest value $I_{\min} = 0.80$ is rarely approached (*cf.* Figure S1). We focus on the results of the tests made with the high instability sampling, but also comment briefly on the tests with uniform fault orientations since this sampling strategy naturally challenges more the assumption of constant shear stress magnitude.

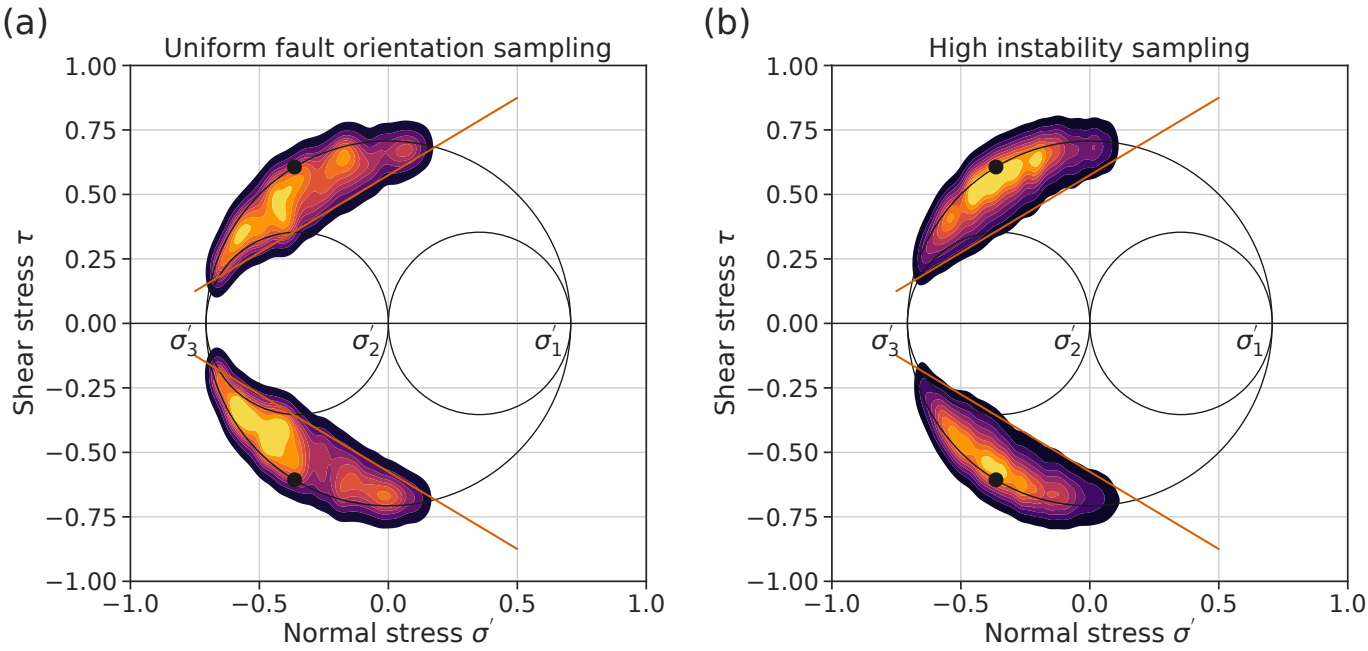

Figure 2: **(a):** Uniform sampling of the fault orientation space with the Mohr-Coulomb failure criterion (red line). **(b):** High instability preferential sampling. The color intensity maps the fault plane density: the brighter/lighter, the denser. The density contours were estimated by smoothing the empirical distribution, resulting in contours artificially showing events outside and in forbidden regions of the Mohr circle. Note: These Mohr circles were drawn with *positive compression* normal stress σ'.

For each data synthesis scenario, we investigate the effect of the size of the data set and noise on the results of the inversion [following previous studies such as Vavryčuk, 2014; Vavryčuk et al., 2015; Martínez-Garzón et al., 2016a]. We recall that a focal mechanism corresponds to a (normalized) moment tensor. Noise is added by rotating the moment tensor about a randomly chosen axis of a randomly chosen angle $\theta \sim \mathcal{U}(-\alpha, +\alpha)$, where $\mathcal{U}$ is the uniform distribution and α is the maximum angle. Thus, α is the parameter controlling the level of noise. We vary the size of the data set from 25 to 250 focal mechanisms, and the noise level from 0° to 60°. Real data sets often exhibit exponentially distributed focal mechanism errors, with errors above 40° seldom encountered [*e.g.* Gephart

and Forsyth, 1984; Hardebeck and Hauksson, 2001]. Therefore, both the uniform distribution of rotation angles and the large rotation angles explored in our experiments are likely to simulate tougher conditions than would exist in real data.

Data synthesis scenario	Description
Scenario 1	Focal mechanisms satisfy the Mohr-Coulomb criterion with $\mu = 0.60$. The fault plane selection algorithm assumes $\mu_A = 0.60$.
Scenario 2	Focal mechanisms satisfy the Mohr-Coulomb criterion with $\mu = 0.60 + \eta$, $\eta \sim \mathcal{U}(-0.4, +0.4)$. The fault plane selection algorithm assumes $\mu_A = 0.60$.
Scenario 3	Most focal mechanisms satisfy the Mohr-Coulomb criterion with $\mu = 0.60 + \eta$, $\eta \sim \mathcal{U}(-0.4, +0.4)$. Focal mechanisms that do not satisfy the failure criterion can be accepted with maximum probability 0.25, and this probability decreases as the fault instability (see Equation (13)) decreases. The fault plane selection algorithm assumes $\mu_A = 0.60$.
Scenario 4	Focal mechanisms satisfy the Mohr-Coulomb criterion with $\mu = 0.75$. The fault plane selection algorithm assumes $\mu_A = 0.60$.
Scenario 5	Focal mechanisms satisfy the Mohr-Coulomb criterion with $\mu = 0.75 + \eta$, $\eta \sim \mathcal{U}(-0.4, +0.4)$. The fault plane selection algorithm assumes $\mu_A = 0.60$.
Scenario 6	Most focal mechanisms satisfy the Mohr-Coulomb criterion with $\mu = 0.75 + \eta$, $\eta \sim \mathcal{U}(-0.4, +0.4)$. Focal mechanisms that do not satisfy the failure criterion can be accepted with maximum probability 0.25, and this probability decreases as the fault instability (see Equation (13)) decreases. The fault plane selection algorithm assumes $\mu_A = 0.60$.

Table 1: Description of the six data synthesis scenarios. Scenarios 4, 5, and 6 are duplicates of 1, 2, and 3, except that the fault plane selection algorithm assumes an incorrect coefficient of friction (*i.e.* $\mu_A \neq \mu$ for scenario 4, and $\mu_A \neq \text{Mean}(\mu)$ for scenarios 5 and 6 with random μ). In all data sets, the smallest fault instability is $I_{\min} = 0.80$ (Equation (13)). $\mathcal{U}$ is the uniform distribution.

The quality of the inverted results is assessed by the following two error parameters:

- ϵ_σ: the 3D rotation angle [Kagan, 1991] between the inverted and the true stress tensors (*i.e.* the smallest rotation angle about *any* axis necessary to superimpose the two tensors),

- $\epsilon_R = |R_{\text{inv}} - R_{\text{true}}|$: the difference between the inverted and the true shape ratios.

To stabilize the results of the tests, we repeat the experiment 50 times for each data set size and noise level and average the errors.

Before analyzing the ensemble of the results over all experiments, we start by presenting in detail the results from a single experiment to clearly describe our analysis. In this experiment, the stress tensor mostly promotes oblique reverse faulting with shape ratio $R = 0.50$ and the data strictly follow the Mohr-Coulomb criterion with $\mu = 0.60$ (data scenario 1, see Table 1). Figure 3 shows the data in the Mohr space and in the P/T space. P and T are the pressure and tension axes of the moment tensors, respectively.

The errors on the inverted parameters show that both methods perform similarly and well in general (*cf.* Figure 4). We analyze the error differences between the two methods to facilitate the comparison ($\Delta\epsilon_\sigma$, $\Delta\epsilon_R$, see Figure 5). The two methods do not produce significant error differences in the estimates of the principal stress directions and direction and magnitude of shear stress. However, noticeable differences appear in the estimate of the shape ratio, and our method produces more accurate results of up to $\Delta\epsilon_R = 0.10$ in some cases. In order to draw general conclusions between the two methods, it is necessary to analyze and interpret the results over the multiple stress states and data scenarios.

We synthesize the results of all experiments in Figure 6. Each 2D map of an error parameter that was given as a function of noise and data set size in Figures 4 and 5 is now summarized by a box plot describing its distribution. We focus the analysis on the error differences between the two

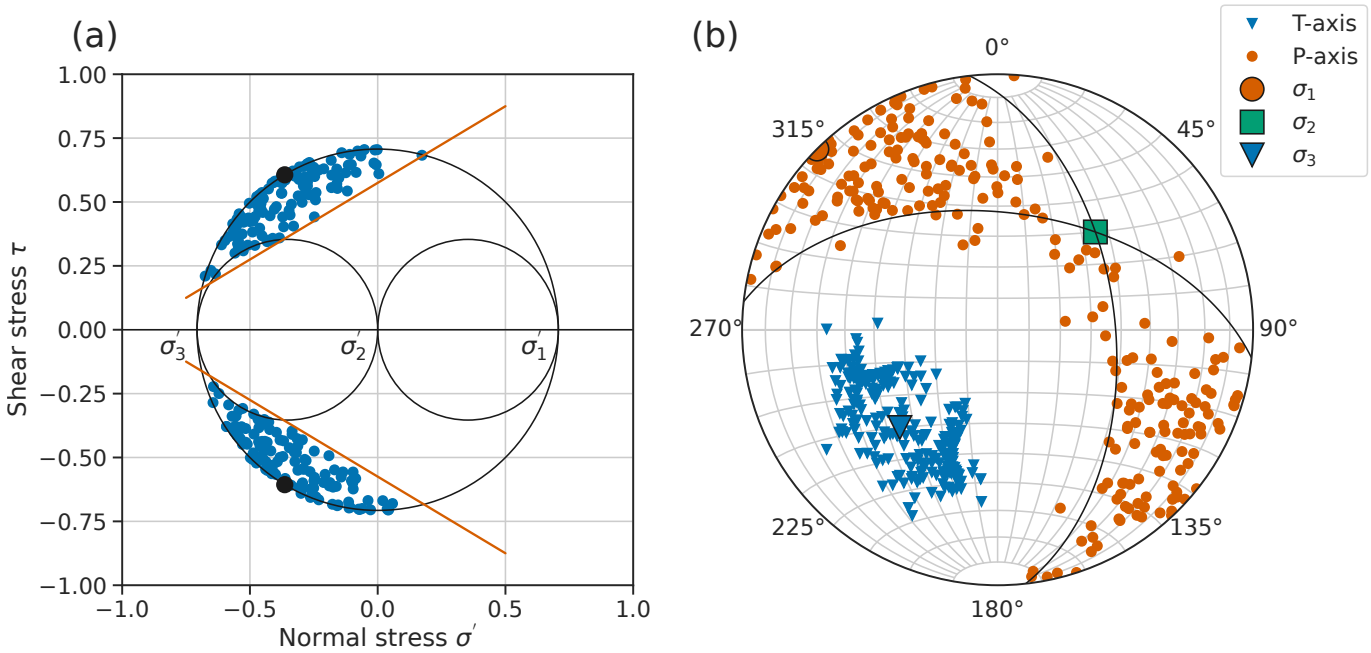

Figure 3: **(a):** Fault planes (blue dots) in the Mohr space. The two red lines indicate the Mohr-Coulomb criterion with $\mu = 0.60$ and cohesion value such that the smallest instability is $I_{\min} = 0.80$ (see Equation (13)). The two most unstable fault planes, the so-called principal faults, are shown by the large black dots (see also the two planes in panel b). σ' is the *positive compression* normal stress. **(b):** Stereographic projection of the P (pressure, red dots) and T (tension, blue inverted triangles) axes of the focal mechanisms. The directions of the three principal stresses (σ_1, σ_2 and σ_3) are also shown. The two black lines are the two principal faults that form a system of two conjugate faults.

methods; the absolute errors are available in the supplementary material (Figure S2) and show that both methods are in general successful at retrieving the correct solution. Overall, the results reveal trends that are similar to that of the experiment presented in detail above. Namely, the two methods produce qualitatively similar estimates of the principal stress directions (Figure 6, column 1). More significant discrepancies exist in the estimates of the shape ratio (Figure 6, column 2), with globally better results with our method.

Our variable shear method appears to produce more accurate results when the data complexity

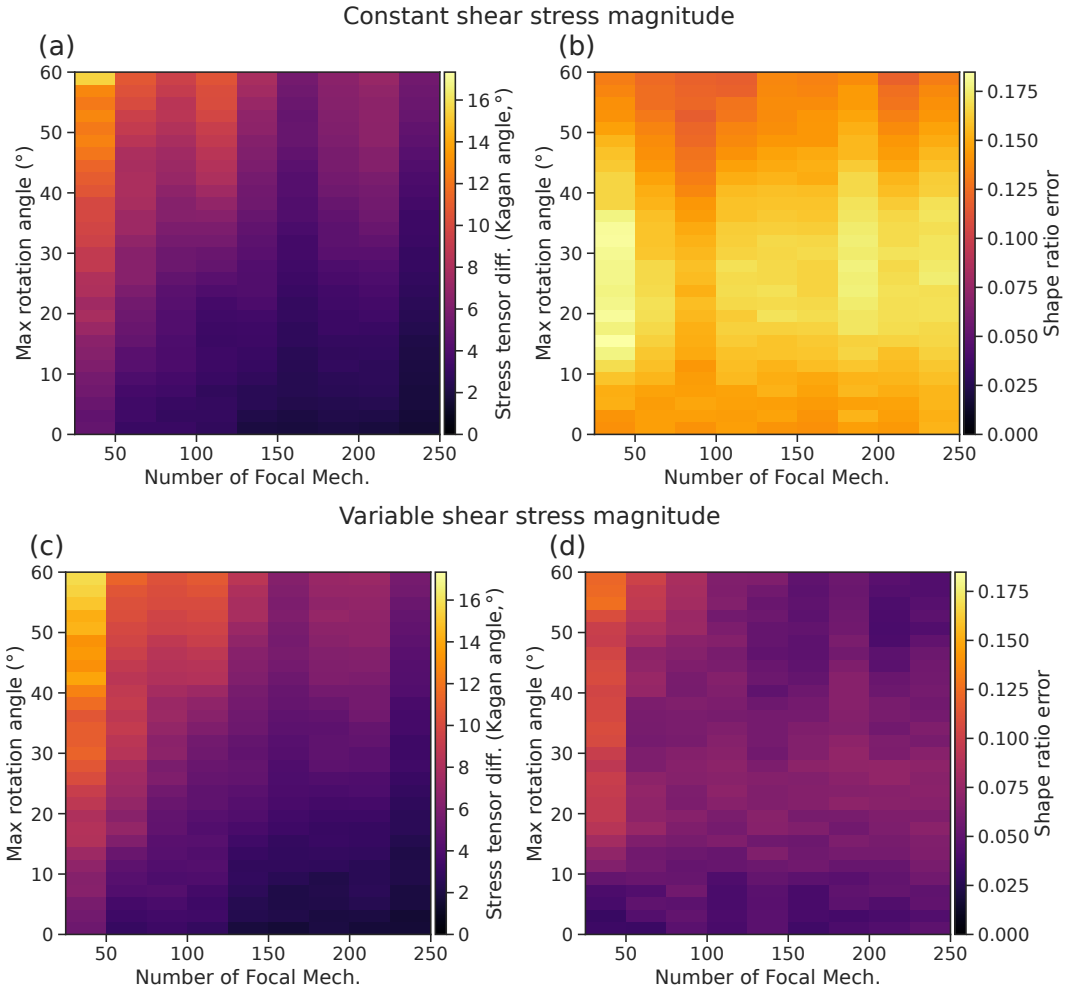

Figure 4: Errors of the inversion results from the stress tensor 1 with $R = 0.50$ (see Table **??**), and data that exactly follow the Mohr-Coulomb failure criterion with $\mu = 0.60$ (Scenario 1 in Table 1) with **a, b:** the constant shear stress magnitude method [Vavryčuk, 2014], and **c, d:** the variable shear stress magnitude method (our method). See the text for additional explanation about the error parameters ϵ_σ (**a, c**), ϵ_R (**b, d**).

is increased (scenario 1 to scenario 6), which might be expected because the data satisfy the assumption of constant shear stress magnitude increasingly worse. A noteworthy feature of these results is that when assuming an incorrect value of coefficient of friction in the fault selection algorithm, our method produces better results (*e.g.* scenario 1 vs. scenario 4, Figure 6). When dealing with

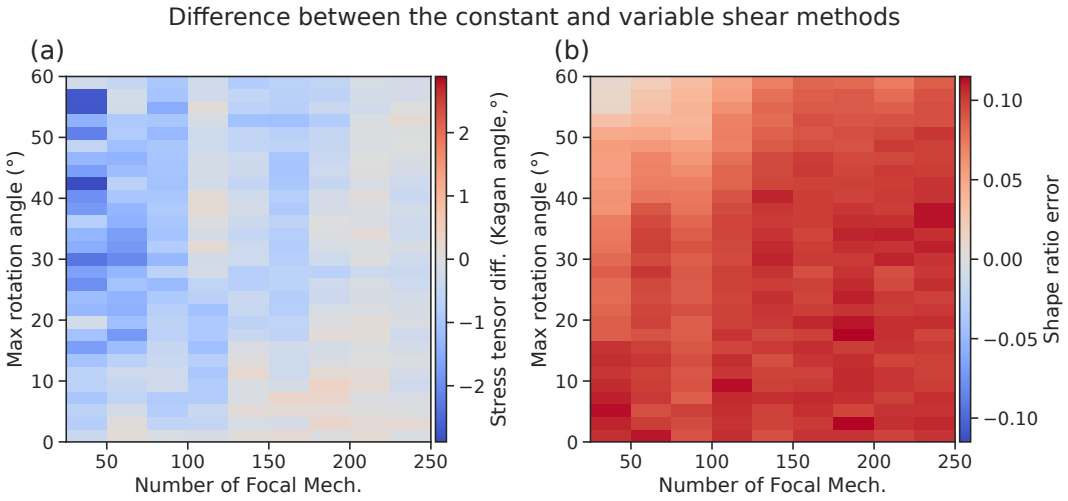

Figure 5: Error differences between the two inversion methods (see Figure 4: right panels minus left panels). Red colors indicate better performances from our variable shear method, whereas blue colors indicate better performances from the constant shear method. Note: beside for the shape ratio, the two methods produce very similar quality results.

real earthquakes, the Mohr-Coulomb failure criterion is only an approximation of the actual failure criterion, and, most likely, whichever value of coefficient of friction μ_A used in the fault selection algorithm is wrong to some extent. Therefore, our scenario 4 might represent more realistic conditions for the inversion methods. We note that Vavryčuk [2014] suggested to choose μ_A as the coefficient of friction that maximizes the average instability I. In this study, we prefer to fix μ_A and keep the number of free parameters to five.

The compact representation of the results shown in Figure 6 does not indicate whether the cases where our variable shear method performs similarly or slightly less well than the constant shear method occur under high noise conditions or small data sets. For that, it is necessary to look at the differences between the error parameters for every experiment, as in Figure 5. We present the comprehensive comparison on scenario 1 and scenario 4 in Figure 7 (other scenarios in Supplementary,

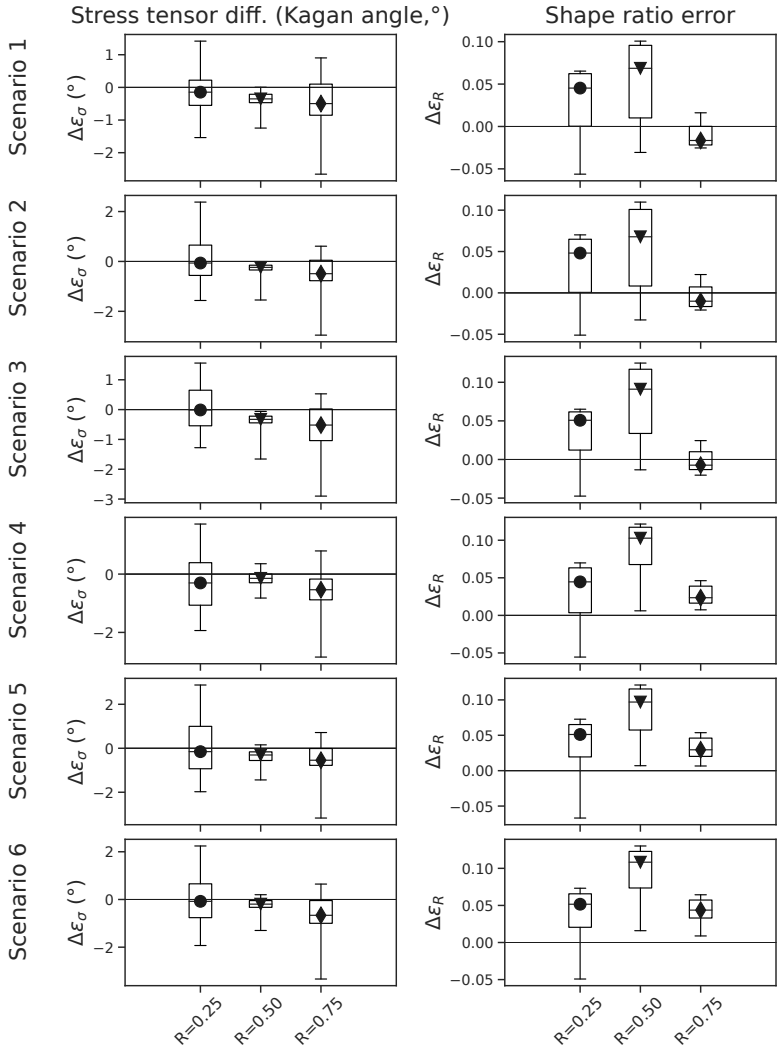

Figure 6: Summary of the error differences between the constant shear and variable shear methods. Each of the two columns shows the distribution of one relative error parameter ($\Delta\epsilon_\sigma$, $\Delta\epsilon_R$). Each row shows the results for a different data scenario (see Table 1). The box plots show the distributions of the relative error parameters for the three shape ratios (filled dots: $R = 0.25$, inverted triangles: $R = 0.50$, diamonds: $R = 0.75$). Symbols indicate the median, limits of the boxes are the first and third quartiles, and whiskers are the 2.5 and 97.5 percentiles (*i.e.* the boxplots cover the 95% confidence interval). Positive values indicate better performances from our variable shear method.

Figure S3). In cases where differences are most significant (for $R = 0.50$ in Figure 7), our variable shear method mostly produces better results, in particular for the shape ratio, even at high noise

levels and small data sets. When the two methods perform similarly over all noise levels and data set sizes, we observe a slight advantage of the constant shear method for low quality data sets. The assumption of constant shear stress magnitude works as a regularizing hypothesis when data are very noisy [Michael, 1984]. However, we note that, in most cases, it becomes advantageous to use the constant shear assumption only at high noise levels ($\alpha > 30°$-$40°$, and uniformly rather than exponentially distributed rotation angles) that may not be reached in real data [Gephart and Forsyth, 1984; Hardebeck and Hauksson, 2001]. Furthermore, the constant shear hypothesis correctly regularizes the problem only if it is a good approximation, which is true here because of our high instability preferential sampling (*cf.* Figure 2). Overall, these tests show that the variable shear method is reliable under noisy conditions, and it often produces more accurate results.

We presented the results obtained with the high instability preferential sampling approach as more unstable faults are likely to be preferentially activated in the crust. An alternative is to sample fault orientations uniformly and accept all the faults that satisfy the Mohr-Coulomb failure criterion (*i.e.* any fault with $I > I_{\min}$). We showed that this sampling strategy seems to prefer low instability faults (*cf.* Figure 2a and Figure S1a) and, therefore, naturally produces data sets for which the constant shear approximation is worse. In the earth, regions with transient changes in the isotropic stress component, for example, because of changes in pore fluid pressure, can create conditions with dominantly low instability faults [*e.g.* Martínez-Garzón et al., 2016b]. We ran a similar series of tests with the uniform orientation sampling approach and drew similar conclusions to those presented here, but the advantage of the variable shear method was enhanced (see results summarized in Figure S4).

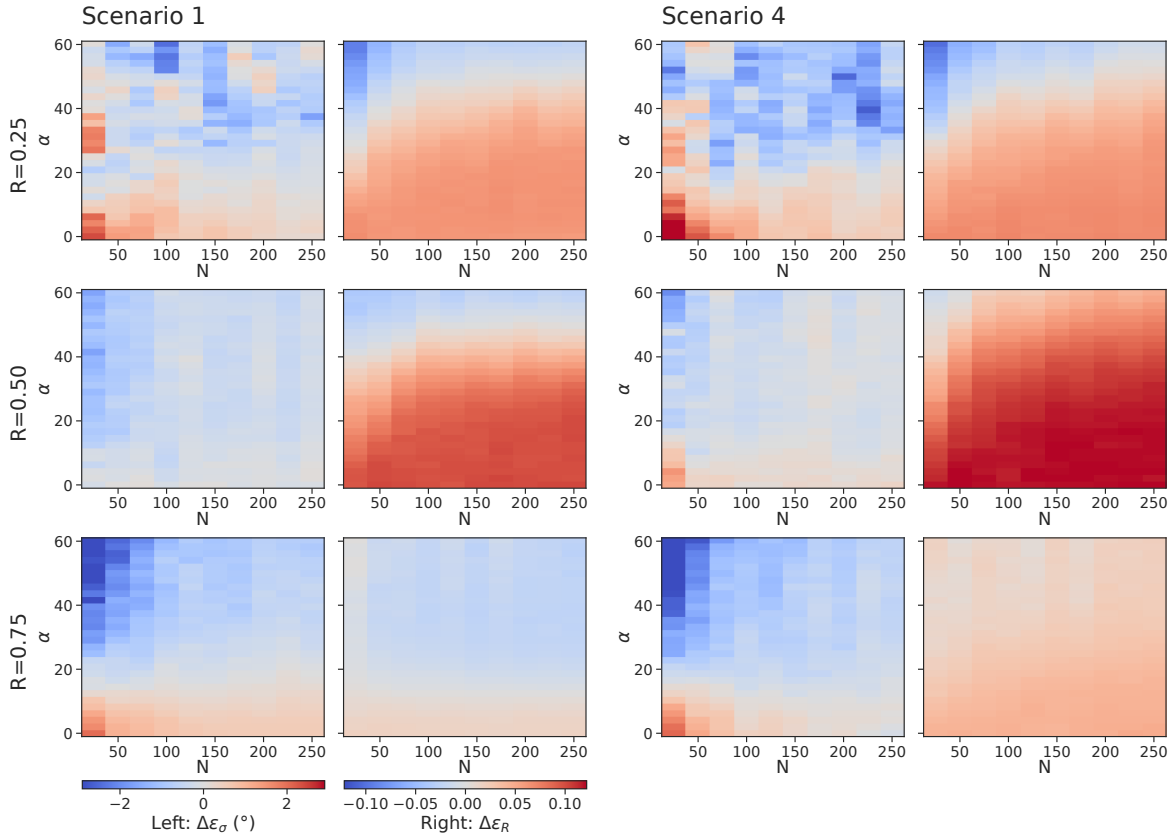

Figure 7: Error differences between the constant and the variable shear stress methods for two data scenarios. **Left:** Scenario 1. **Right:** Scenario 4. Each 2-panel subfigure is similar to Figure 5 (see also color bar labels for meaning of each subpanel). Figure axis labels are the same as Figure 5. Red colors indicate better performances from our variable shear stress method, whereas blue colors indicate that the constant shear stress method does better. We recall that scenarios 1 and 4 only differ by the coefficient of friction μ_A in the fault plane selection algorithm (scenario 1 = assume correct value, scenario 4 = assume incorrect value).

4. Application to Real Data

We demonstrate the applicability of our variable shear method to real data on two data sets: the Southern California data set (Section 4.1), and the Geysers geothermal field, California, data set (Section 4.2). The latter was chosen because it is known to feature fluid induced earthquakes [*e.g.* Martínez-Garzón et al., 2013] and, therefore, stress conditions that are more likely to produce

discrepancies between the constant and variable shear methods, as discussed at the end of Section 3.

In the following application, we not only compare the iterative constant [Vavryčuk, 2014] and variable shear methods (the proposed method) but also the regular linear method [*i.e.* constant shear and no fault plane selection, Michael, 1984]. The uncertainties are computed by bootstrap resampling the data set 2000 times. Each bootstrap replica contains the same number of focal mechanisms as in the original data set, but some focal mechanisms can be repeated several times while others can be absent from the resampled data set. For the regular linear method with no fault selection criterion, the fault plane of a given focal mechanism is randomly selected out of the two nodal planes. We chose to include the linear method in the comparison because it is known to produce accurate confidence intervals with bootstrap resampling [especially on very noisy data sets, Hardebeck and Hauksson, 2001], and therefore it is worth checking if all these methods yield statistically significant solutions.

4.1. Southern California

The Southern California data set contains 298 $M > 1$ earthquake focal mechanisms [see Hauksson et al., 2012; Yang et al., 2012, and Data and Resources]. We selected focal mechanisms within a region of limited extent (most of the earthquakes are within a $10\,\mathrm{km}\times10\,\mathrm{km}$ area, *cf.* Figure 8a). The data set shows mostly E/W horizontal tension axes and N/S horizontal pressure axes (see Figure 8b). The focal mechanisms indicate predominantly strike-slip faulting earthquakes, but also oblique-reverse earthquakes, and a few oblique-normal earthquakes [see classification of focal mechanisms in the Kaverina diagram, Kaverina et al., 1996, see Figure 8c].

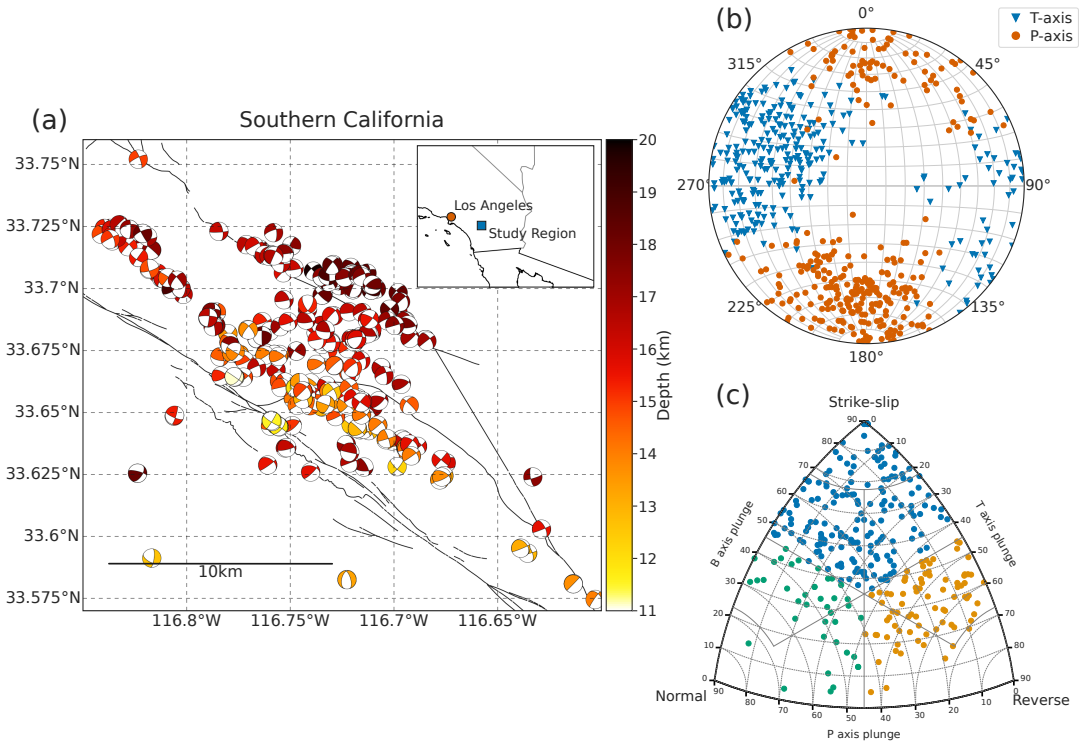

Figure 8: Southern California data set. **(a):** Lower hemisphere focal mechanisms colored by depth. **(b):** P (red dots) and T axes (blue inverted triangles). **(c):** Representation of the focal mechanisms in the Kaverina diagram. The dominant faulting style is strike-slip, with also many oblique reverse faulting earthquakes, and some oblique normal faulting earthquakes.

The stress inversion results are presented in Figure 9 and Table 2. The three methods retrieve the same directions of principal stresses, which is often observed when comparing different inversion techniques [*e.g.* Vavryčuk et al., 2015, and our synthetic tests]. The principal directions indicate a stress state close to the Andersonian strike-slip regime, with almost horizontal N/S most compressive stress σ_1 and E/W least compressive stress σ_3. Significant differences in the inverted shape ratio R are observed between the linear and the two iterative methods, whereas the latter two methods predict shape ratios that are similar to within their uncertainties. The iterative methods produce an

average angle between the predicted resolved shear stresses and observed slip directions, β [the misfit measure used in Michael, 1984], that is smaller than that of the linear method by about 4°-5°. Thus, the iterative methods produce solutions that follow better the Wallace-Bott hypothesis, but, given that β is sensitive to noise in the data set, this difference is too small to confidently assert that these solutions are better than that of the linear method. However, focal mechanisms revealed that earthquakes were mostly a mix of strike-slip and oblique-reverse events, indicating a transpression regime. When σ_1 and σ_3 are (nearly) horizontal (as in Figure 9a), such transpression regime is described by $R > 0.50$. The shape ratios $R = 0.74$ and $R = 0.84$ obtained by the two iterative methods better describe a transpression regime than the $R = 0.51$ estimated by the linear method. Thus, we can still be confident that the use of a fault plane selection algorithm helped the two iterative methods produce more accurate results about the true stress state.

	Linear	Iterative constant shear	Iterative variable shear
$\hat{\sigma}_1$ (az., pl.)	(189.0°, 15.4°)	(189.3°, 15.7°)	(188.2°, 20.8°)
95% CI	(183.0°-197.8°, 5.2°-26.7°)	(183.3°-197.8°, 5.4°-26.7°)	(181.2°-197.5°, 9.6°-33.2°)
$\hat{\sigma}_2$ (az., pl.)	(67.7°, 62.0°)	(65.4°, 63.3°)	(57.6°, 59.7°)
95% CI	(41.9°-95.4°, 50.2°-74.4°)	(35.5°-93.5°, 51.2°-75.7°)	(35.1°-84.6°, 42.8°-70.7°)
$\hat{\sigma}_3$ (az., pl.)	(285.7°, 22.7°)	(285.5°, 21.1°)	(286.6°, 21.0°)
95% CI	(273.4°-298.0°, 10.8°-34.6°)	(273.3°-298.0°, 8.3°-33.0°)	(273.4°-303.2°, 10.8°-38.1°)
R	0.51	0.74	0.84
95% CI	(0.43, 0.59)	(0.70, 0.81)	(0.76, 0.87)

Table 2: Inverted parameters from the Southern California data set (Figure 9). The principal stress directions $\hat{\sigma}_i$s are given as (azimuth, plunge). The 95% confidence interval of each parameter is also given.

4.2. The Geysers Geothermal Field

The Geysers geothermal field data set contains 116 earthquake focal mechanisms [NCEDC, 2014, and see Data and Resources]. The data were selected inside a narrow area (1 km×2 km, see Fig-

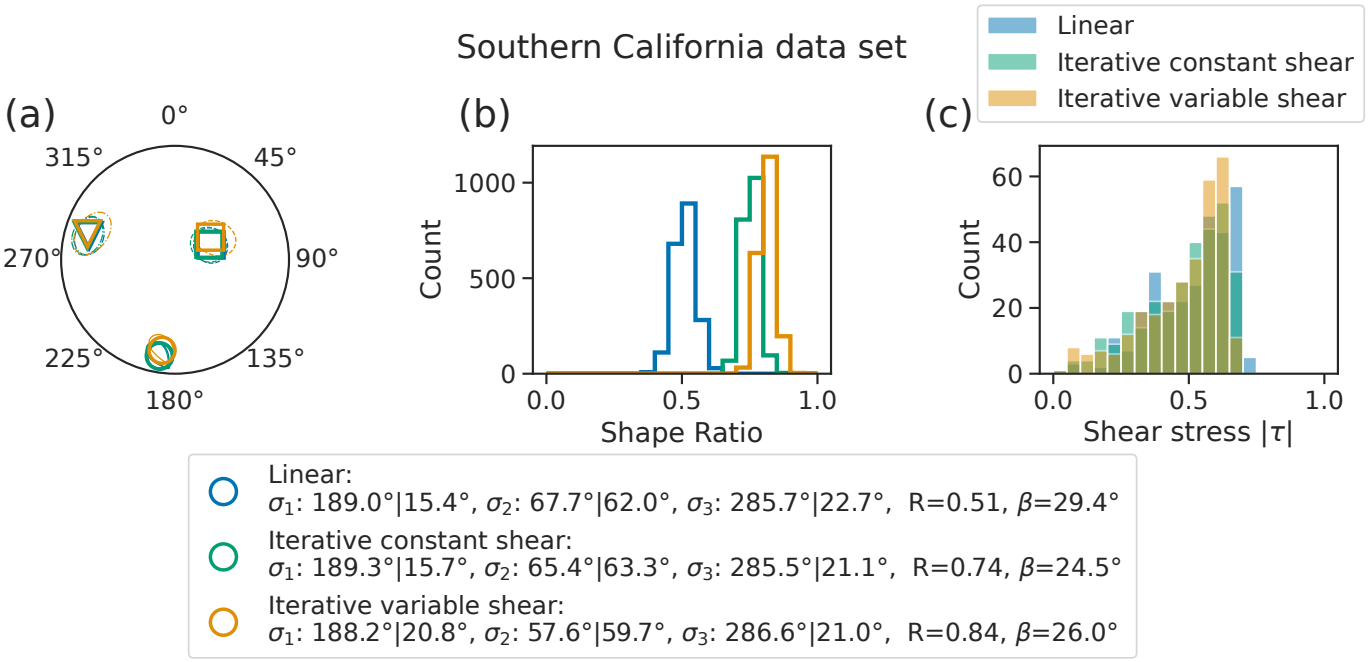

Figure 9: Southern California results. **(a):** Stereographic projection of the directions of the principal stresses. Circle: σ_1, most compressive stress; square: σ_2, intermediate stress; triangle: σ_3, least compressive stress. See the legend for the azimuth—plunge values. The 95% confidence intervals are shown. **(b):** Distribution of inverted shape ratios on bootstrapped data sets. **(c)**: Distribution of resolved shear stress magnitudes.

ure 10a) and between 2010-12-01 and 2011-04-01 because this seismicity is known to be associated with an episode of high fluid injection in two nearby wells [Martínez-Garzón et al., 2013], *i.e.* under high pore fluid pressure. Such conditions promote a wide variety of fault instability levels [as in the uniform fault orientation sampling explored in supplementary, and, *e.g.* Martínez-Garzón et al., 2016b] and thus contribute to producing a wide variety of shear stress magnitudes on faults, which should lead to some discrepancies between the constant and variable shear inversion methods. The data set mostly shows W-NW/E-SE tension axes and vertical pressure axes (*cf.* Figure 10b). The Kaverina diagram indicates that most earthquakes occur on normal faults, mixed with some oblique-normal earthquakes (see Figure 10c).

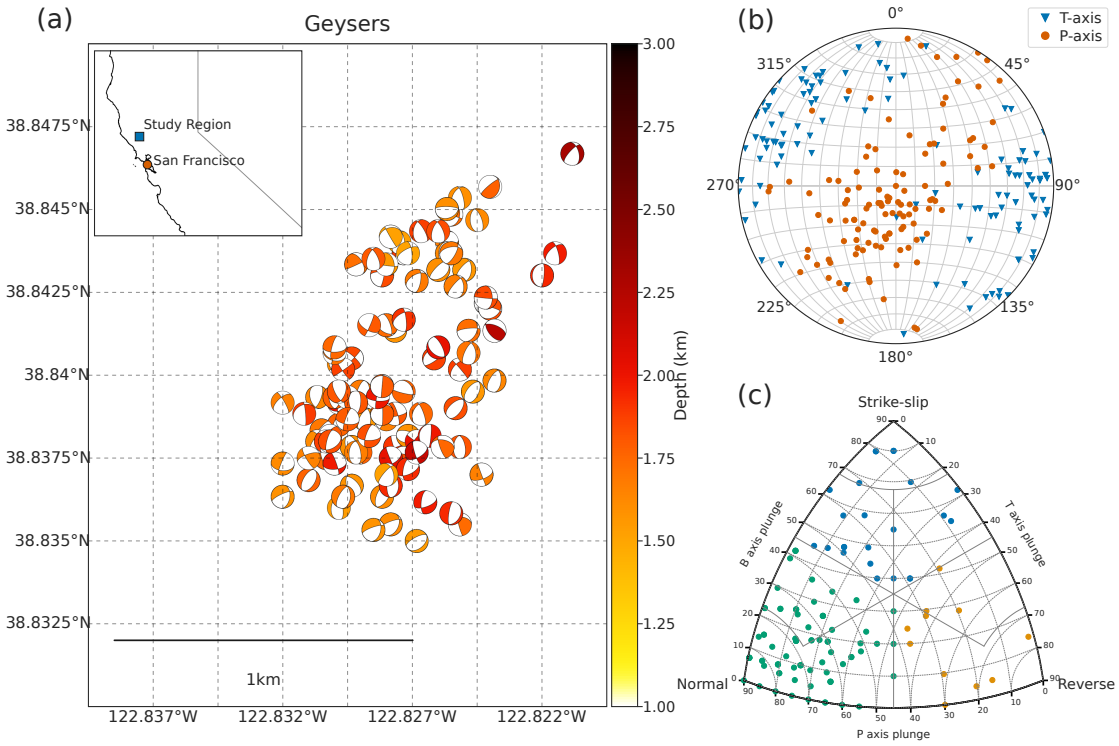

Figure 10: The Geysers geothermal field data set. **(a):** Lower hemisphere focal mechanisms colored by depth. **(b):** P (red dots) and T axes (blue inverted triangles). **(c):** Representation of the focal mechanisms in the Kaverina diagram. The dominant faulting style is normal, with some oblique normal/strike-slip faulting earthquakes, and few reverse faulting earthquakes.

The directions of the principal stresses are similarly estimated by the three inversion methods (see Figure 11a and Table 3). Minor differences remain within the 95% confidence interval of each method (see Table 3). Clearer differences are seen in the inverted shape ratios (*cf.* Figure 11b), the three methods giving different estimates but with considerable overlap of their confidence intervals. Our variable shear method and the linear method seem to produce statistically meaningful differences, with a significantly higher estimate of the shape ratio with our method, $R = 0.69$, vs. $R = 0.43$ for the linear method. Even though the shape ratio distributions from the two iterative methods do

not overlap as much as in the Southern California data set, the overlap is still too large to make the differences statistically significant. We note that the shape ratios inverted from the original data set, $R = 0.61$ for the constant shear method vs. $R = 0.69$ for the variable shear method, indicate a difference of about 0.1, which is in the range of error difference observed in the synthetic tests between the two methods. Using the mean shear/slip angle β to evaluate the quality of each solution is again difficult as the three values are similar and probably not meaningfully different given noise in the data.

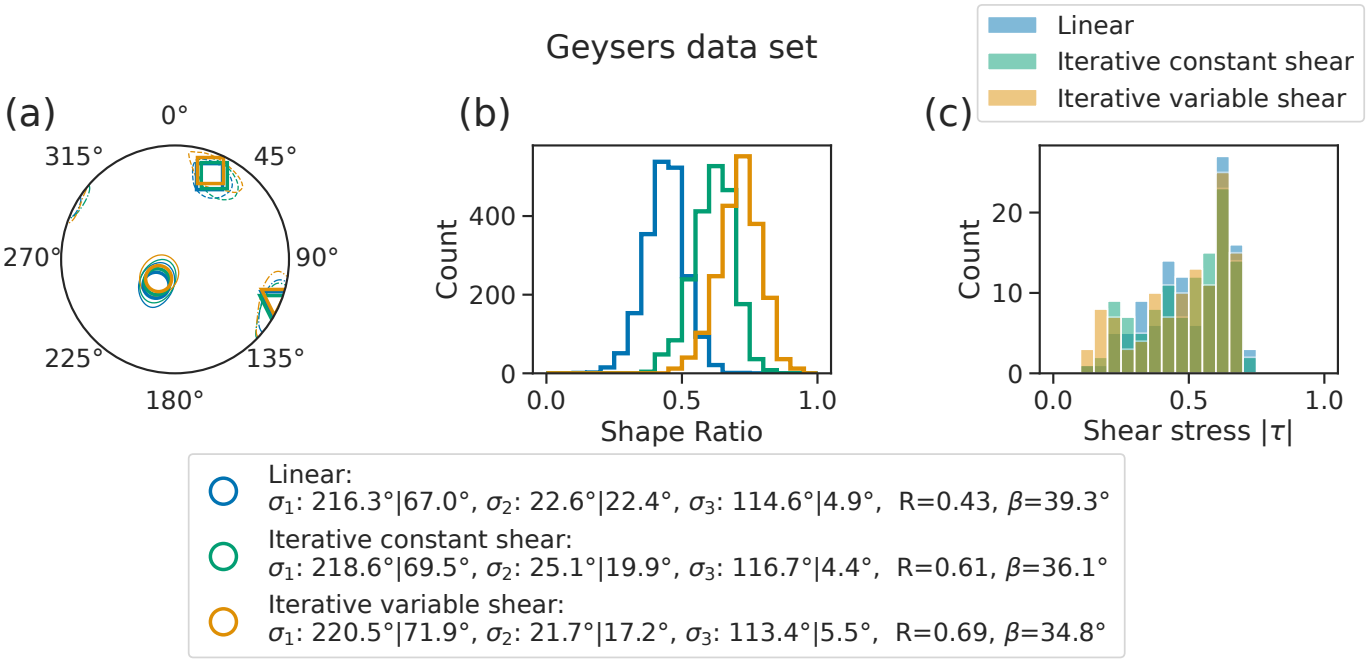

Figure 11: The Geysers results. **(a):** Stereographic projection of the directions of the principal stresses. Circle: σ_1, most compressive stress; square: σ_2, intermediate stress; triangle: σ_3, least compressive stress. See the legend for the azimuth—plunge values. The 95% confidence intervals are shown. **(b):** Distribution of inverted shape ratios on bootstrapped data sets. **(c)**: Distribution of resolved shear stress magnitudes.

	Linear	Iterative constant shear	Iterative variable shear
$\hat{\sigma}_1$ (az., pl.)	(216.3°, 67.0°)	(218.6°, 69.5°)	(220.5°, 71.9°)
95% CI	(181.5°-257.1°, 50.9°-83.6°)	(177.3°-267.7°, 54.0°-86.1°)	(161.6°-291.1°, 57.9°-88.6°)
$\hat{\sigma}_2$ (az., pl.)	(22.6°, 22.4°)	(25.1°, 19.9°)	(21.7°, 17.2°)
95% CI	(11.0°-38.4°, 9.0°-38.8°)	(12.8°-43.5°, 6.2°-35.6°)	(7.4°-43.3°, 3.5°-31.0°)
$\hat{\sigma}_3$ (az., pl.)	(114.6°, 4.9°)	(116.7°, 4.4°)	(113.4°, 5.5°)
95% CI	(101.3°-129.3°, 0.3°-16.4°)	(103.1°-133.7°, 0.3°-15.5°)	(96.8°-132.8°, 0.3°-19.9°)
R	0.43	0.61	0.69
95% CI	(0.29, 0.58)	(0.45, 0.75)	(0.54, 0.85)

Table 3: Inverted parameters from the Geysers data set (Figure 11). The principal stress directions $\hat{\sigma}_i$s are given as (azimuth, plunge). The 95% confidence interval of each parameter is also given.

5. On the Applicability of the Proposed Method to Real Data, and Future Applications

Despite lacking ground truth, we argue that our variable shear method is better suited to analyze the Geysers data set because of its widely distributed shear stress magnitudes. The fraction of faults with a given shear $|\tau|$ does not decrease smoothly with $|\tau|$, as is the case for the Southern California data set (compare Figure 9c and Figure 11c). When converting these shear stresses into fault instabilities, it is more apparent that the Geysers data set contains more non-optimally oriented faults (see Figure S5). Comparing the discrepancy between the constant and the variable shear methods constitutes a way of measuring the validity of the constant shear approximation. However, the inhomogeneity of inverted shear stress magnitudes has also been used to assess the validity of the uniform stress assumption, namely that variations in shear stress magnitudes are a consequence of stress heterogeneities [*e.g.* Michael, 1984]. Nevertheless, our synthetic tests showed that the proposed method was not prone to data overfitting, and therefore we believe that our method helps retrieve more accurately the uniform component of a stress field. Rigorous testing of this idea remains to be done [such as in Michael, 1991], but is out of the scope of this first study. Beside, we note that, in reality, low instability fault planes might rupture with a non-negligible tensile component [*e.g.*

Vavryčuk, 2011] that our algorithm is not designed to deal with. Finally, it is important to mention that methods aiming at finding a heterogeneous stress tensor have been developed [Hardebeck and Michael, 2006; Martínez-Garzón et al., 2014] and that the algorithm described here could be implemented in these methods. Together, these would remove the necessity for the assumptions of constant shear stress magnitudes and homogeneity of the stress tensor.

6. Summary and Concluding Remarks

In Section 2.1, we introduced the stress tensor inversion problem and presented the underlying assumptions and drawbacks. In Section 2.2, we introduced an iterative inversion method that explicitly accounts for variable shear stress magnitudes. This method is built upon the linear inversion due to Michael [1984], and follows the fault selection algorithm from previous studies [*e.g.* Lund and Slunga, 1999; Vavryčuk, 2014] to deal with focal mechanism data sets where the true fault planes are generally unknown. The proposed method effectively solves the non-linear inverse problem, where shear stress is a non-linear function of the stress tensor, by repeating the linear inversion described in Michael [1984] with shear stress magnitudes estimated from the stress tensor computed in the previous iteration.

We conducted a series of synthetic tests on realistic data sets where the assumption of constant shear stress magnitude is a fair approximation (see discussion on data sampling in Figure 2). We showed that the proposed variable shear method was similarly robust to noise and data set size as its constant shear counterpart [Vavryčuk, 2014] based on synthetic tests that explored different stress regimes and different assumptions on the data (*cf.* Section 3). The results showed that our variable

shear method often produce more accurate solutions, in particular in the estimate of the shape ratio, and that otherwise the two iterative methods perform similarly (see Figure 6). The regularization due to the assumption that all shear stress magnitudes are the same [Michael, 1984] did not produce any significant differences between the two methods, and only favored the constant shear method for very high noise conditions (α >30°-40°) that are unlikely to be encountered in real data sets (see Figure 7). Differences between the two methods became more apparent as the assumptions underlying the data synthesis got more complex (*e.g.* coefficient of friction is not the same on all faults). Disregarding whether the Mohr-Coulomb failure criterion describes well the data or not, our tests suggested that the variable shear method was more robust to erroneous assumptions on the coefficient of friction in the fault plane selection algorithm. Nevertheless, differences between the two methods remained small and likely to not be statistically significant in real data applications where the ground truth is unknown and uncertainties have to be taken into account.

We applied our method to real data sets (from Southern California and the Geysers geothermal field, see Section 4) and showed that differences between the two iterative methods were within the 95% confidence interval of each other. Uncertainties were estimated with the bootstrap resampling method [Efron and Tibshirani, 1986]. Thus, our study showed that the primary interest of the proposed method is in relying on fewer assumptions in the stress inversion methodology. It has been argued that a wide distribution of shear stress magnitudes could reflect the inadequacy of the uniform stress model [Michael, 1984], although there exists physical conditions, such as high pore fluid pressure environments [*e.g.* Martínez-Garzón et al., 2016b] or heterogeneous coefficients of friction [Collettini et al., 2009], where shear stress magnitudes are not closely clustered around a single value. Our proposed method therefore fully handles all data sets that can be described by shear earthquakes

in a uniform stress state, and we speculate that it will help resolve the contribution of stress heterogeneities to data misfit. Even though this study did not explore the effects of stress heterogeneities on the inversion results, our variable shear method can be used jointly with techniques that deal with these. For example, stress heterogeneities originating from interactions between earthquakes can be removed by declustering the earthquake catalog from which focal mechanisms are computed [*e.g.* Martínez-Garzón et al., 2016a], or our proposed method can be included in a broader inversion scheme that aims at resolving the stress state as a function of space [*e.g.* Hardebeck and Michael, 2006].

Running the synthetic tests and real data applications with our implementation of the constant and variable shear iterative method in the Python package ILSI (see Data and Resources) showed that the variable shear method took only 1.5 to 2 times longer than the constant shear method. This modest runtime increase makes the proposed method well-suited for large scale problems, and a good candidate for improving current non-homogeneous stress inversions relying on a linear inversion (SATSI, Hardebeck and Michael [2006], or its Matlab implementation MSATSI, Martínez-Garzón et al. [2014]).

Data and Resources

The Southern California focal mechanisms were obtained from the Southern California Earthquake Data Center at `https://scedc.caltech.edu/data/alt-2011-yang-hauksson-shearer.html` [we used the 2011-2013 catalog, Hauksson et al., 2012; Yang et al., 2012]. The Geysers geothermal field focal mechanisms were obtained from the Northern California Earthquake Data Center at

https://www.ncedc.org/ncedc/catalog-search.html [NCEDC, 2014]. In the real data applications, we restricted the catalog to the region displayed in Figures 8 and 10. The Kaverina diagrams were produced using the plotting routine from FMC [https://github.com/Jose-Alvarez/FMC, version 1.6, last accessed November 2021, Álvarez-Gómez, 2019]. Faults in Figure 9 were taken from the USGS data base (https://www.usgs.gov/programs/earthquake-hazards/faults, last visited in February 2022).

The Python package ILSI, available at https://github.com/ebeauce/ILSI, implements the variable shear method proposed here and the constant shear method described in Vavryčuk [2014]. The repository also provides the scripts to reproduce our figures (version 1.0.3, last accessed February 2022).

The supplemental material includes figures to show the differences in fault instabilities produced by the two fault sampling strategies described in this manuscript (Figure S1), additional results from the synthetic tests presented here (Figures S2, S3), results from different tests (Figure S4), and the fault instabilities of the Southern California and Geysers data sets used in the real data applications (Figure S5).

Acknowledgements

The authors thank Andrew Michael and one anonymous reviewer for helping considerably improve the study and the manuscript. This project has received funding from the European Research Council (ERC) under the European Union's Horizon H2020 research and innovation program (grant

agreement No 742335). E.B. was also supported by funds associated with RvdH's Schlumberger chair.

References

J. A. Álvarez-Gómez. Fmc—earthquake focal mechanisms data management, cluster and classification. *SoftwareX*, 9:299–307, 2019.

J. Angelier. Determination of the mean principal directions of stresses for a given fault population. *Tectonophysics*, 56(3-4):T17–T26, 1979.

J. Angelier, A. Tarantola, B. Valette, and S. Manoussis. Inversion of field data in fault tectonics to obtain the regional stress—i. single phase fault populations: a new method of computing the stress tensor. *Geophysical Journal International*, 69(3):607–621, 1982.

M. H. P. Bott. The mechanics of oblique slip faulting. *Geological magazine*, 96(2):109–117, 1959.

E. Carey et al. Analyse theorique et numerique d'un modele mecanique elementaire applique a l'etude d'une population de failles. 1974.

C. Collettini, A. Niemeijer, C. Viti, and C. Marone. Fault zone fabric and fault weakness. *Nature*, 462(7275):907–910, 2009.

B. Efron and R. Tibshirani. Bootstrap methods for standard errors, confidence intervals, and other measures of statistical accuracy. *Statistical science*, pages 54–75, 1986.

J. W. Gephart. Fmsi: A fortran program for inverting fault/slickenside and earthquake focal mechanism data to obtain the regional stress tensor. *Computers & Geosciences*, 16(7):953–989, 1990.

J. W. Gephart and D. W. Forsyth. An improved method for determining the regional stress tensor using earthquake focal mechanism data: application to the san fernando earthquake sequence. *Journal of Geophysical Research: Solid Earth*, 89(B11):9305–9320, 1984.

J. L. Hardebeck and E. Hauksson. Stress orientations obtained from earthquake focal mechanisms: what are appropriate uncertainty estimates? *Bulletin of the Seismological Society of America*, 91 (2):250–262, 2001.

J. L. Hardebeck and A. J. Michael. Damped regional-scale stress inversions: Methodology and examples for southern california and the coalinga aftershock sequence. *Journal of Geophysical Research: Solid Earth*, 111(B11), 2006.

E. Hauksson, W. Yang, and P. M. Shearer. Waveform relocated earthquake catalog for southern california (1981 to june 2011). *Bulletin of the Seismological Society of America*, 102(5):2239–2244, 2012.

Y. Kagan. 3-d rotation of double-couple earthquake sources. *Geophysical Journal International*, 106 (3):709–716, 1991.

A. Kaverina, A. Lander, and A. Prozorov. Global creepex distribution and its relation to earthquake-source geometry and tectonic origin. *Geophysical Journal International*, 125(1):249–265, 1996.

B. Lund and R. Slunga. Stress tensor inversion using detailed microearthquake information and stability constraints: Application to ölfus in southwest iceland. *Journal of Geophysical Research: Solid Earth*, 104(B7):14947–14964, 1999.

P. Martínez-Garzón, M. Bohnhoff, G. Kwiatek, and G. Dresen. Stress tensor changes related to

fluid injection at the geysers geothermal field, california. *Geophysical Research Letters*, 40(11): 2596–2601, 2013.

P. Martínez-Garzón, G. Kwiatek, M. Ickrath, and M. Bohnhoff. Msatsi: A matlab package for stress inversion combining solid classic methodology, a new simplified user-handling, and a visualization tool. *Seismological Research Letters*, 85(4):896–904, 2014.

P. Martínez-Garzón, Y. Ben-Zion, N. Abolfathian, G. Kwiatek, and M. Bohnhoff. A refined methodology for stress inversions of earthquake focal mechanisms. *Journal of Geophysical Research: Solid Earth*, 121(12):8666–8687, 2016a.

P. Martínez-Garzón, V. Vavryčuk, G. Kwiatek, and M. Bohnhoff. Sensitivity of stress inversion of focal mechanisms to pore pressure changes. *Geophysical Research Letters*, 43(16):8441–8450, 2016b.

A. J. Michael. Determination of stress from slip data: faults and folds. *Journal of Geophysical Research: Solid Earth*, 89(B13):11517–11526, 1984.

A. J. Michael. Stress rotation during the coalinga aftershock sequence. *Journal of Geophysical Research: Solid Earth*, 92(B8):7963–7979, 1987a.

A. J. Michael. Use of focal mechanisms to determine stress: a control study. *Journal of Geophysical Research: Solid Earth*, 92(B1):357–368, 1987b.

A. J. Michael. Spatial variations in stress within the 1987 whittier narrows, california, aftershock sequence: New techniques and results. *Journal of Geophysical Research: Solid Earth*, 96(B4): 6303–6319, 1991.

NCEDC. Northern California Earthquake Data Center. UC Berkeley Seismological Laboratory., 2014.

S. Stein and M. Wysession. *An introduction to seismology, earthquakes, and earth structure*. John Wiley & Sons, 2009.

A. Tarantola and B. Valette. Generalized nonlinear inverse problems solved using the least squares criterion. *Reviews of Geophysics*, 20(2):219–232, 1982.

V. Vavryčuk. Tensile earthquakes: Theory, modeling, and inversion. *Journal of Geophysical Research: Solid Earth*, 116(B12), 2011.

V. Vavryčuk. Iterative joint inversion for stress and fault orientations from focal mechanisms. *Geophysical Journal International*, 199(1):69–77, 2014.

V. Vavryčuk, F. Bouchaala, and T. Fischer. High-resolution fault image from accurate locations and focal mechanisms of the 2008 swarm earthquakes in west bohemia, czech republic. *Tectonophysics*, 590:189–195, 2013.

V. Vavryčuk, M. Beer, I. Kougioumtzoglou, E. Patelli, and I. Au. Earthquake mechanisms and stress field. *Encyclopedia of earthquake engineering*, pages 728–746, 2015.

R. E. Wallace. Geometry of shearing stress and relation to faulting. *The Journal of geology*, 59(2): 118–130, 1951.

W. Yang, E. Hauksson, and P. M. Shearer. Computing a large refined catalog of focal mechanisms for southern california (1981–2010): Temporal stability of the style of faulting. *Bulletin of the Seismological Society of America*, 102(3):1179–1194, 2012.

Supplemental Material of "An Iterative Linear Method with Variable Shear Stress Magnitudes for Estimating the Stress Tensor from Earthquake Focal Mechanism Data: Method and Examples"

Eric Beaucé[1,3], Robert D. van der Hilst[1], and Michel Campillo[2,1]

[1]Department of Earth, Atmospheric, and Planetary Sciences, Massachusetts Institute of Technology, Cambridge, MA, United States
[2]Institut des Sciences de la Terre, Université Grenoble Alpes, Grenoble, France
[3]Lamont-Doherty Earth Observatory, Columbia University, NY, United States

Description of the Content

Figures S1 to S7.

Content

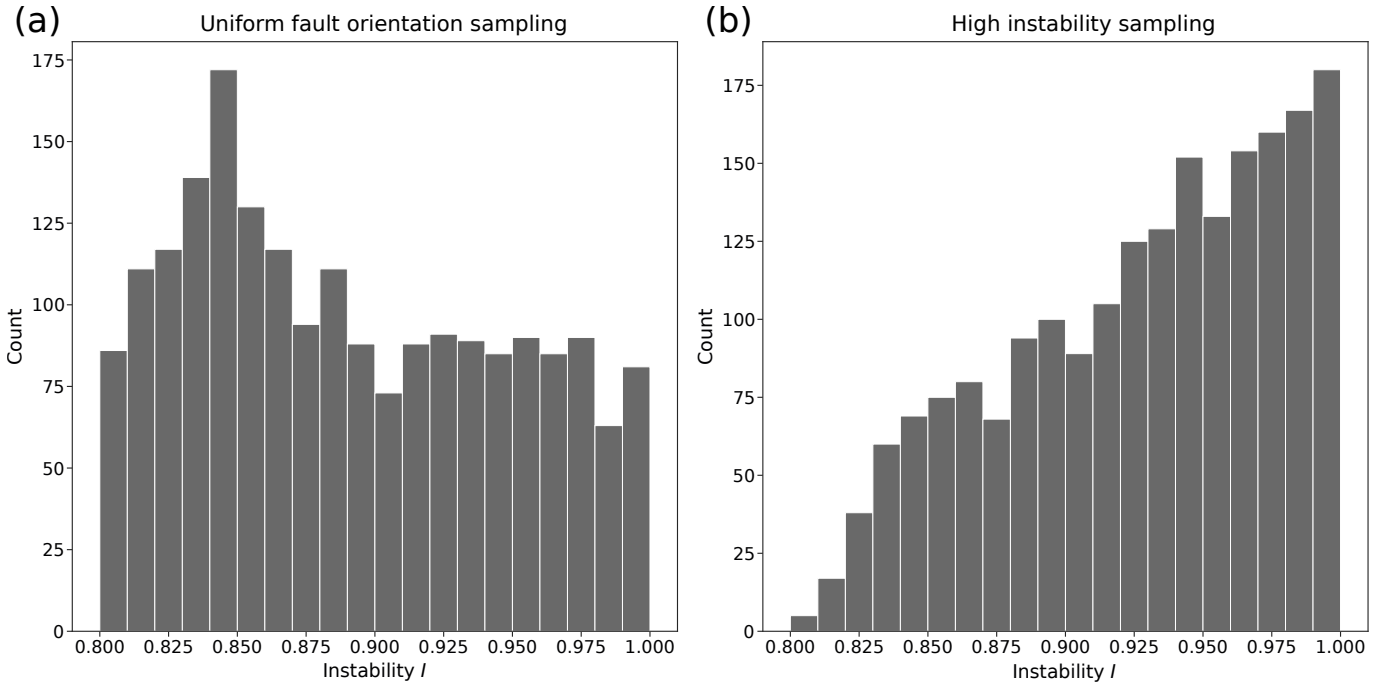

Figure S1: Distribution of fault instabilities for **(a):** the uniform fault orientation sampling, and **(b):** the high instability preferential sampling.

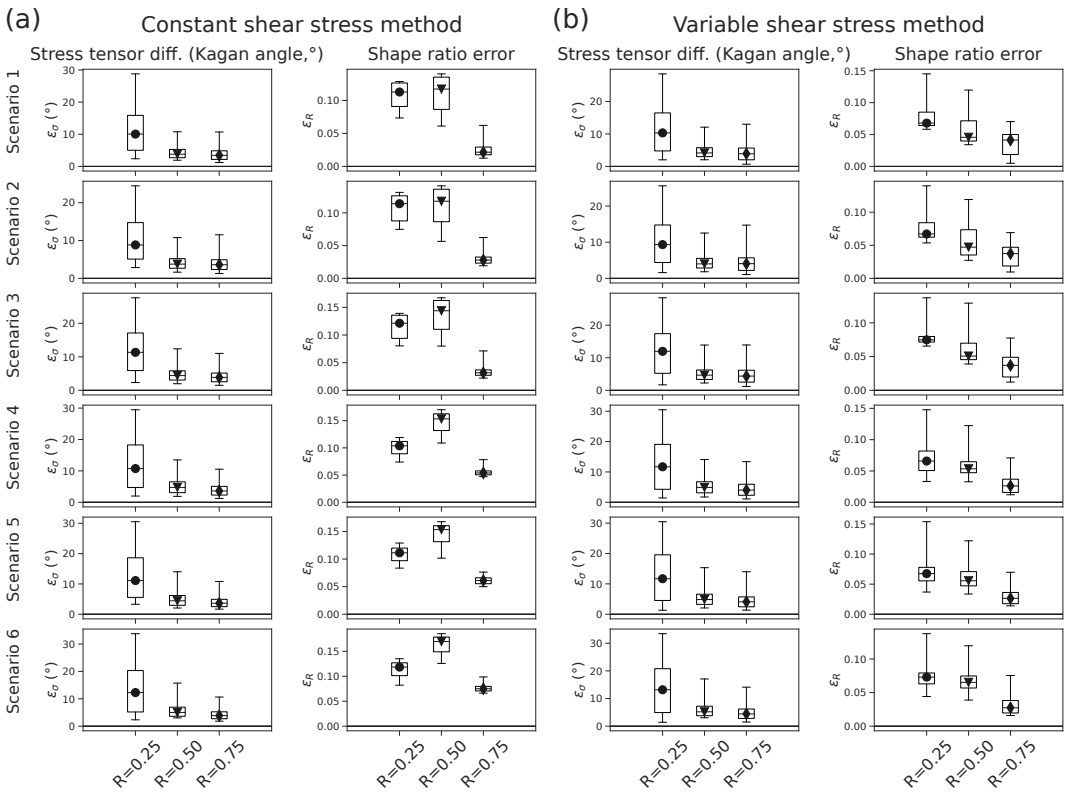

Figure S2: Summary of the errors of **(a):** the constant shear method and **(b):** the variable shear method. Each column shows the distribution of one error parameter (ϵ_σ and ϵ_R), represented by a box plot. Each row shows the results for a different data scenario (see Table 1 in the main manuscript). The box plots show the results for the three shape ratio values (filled dots: $R = 0.25$, inverted triangles: $R = 0.50$; diamonds: $R = 0.75$). Symbols indicate the median, limits of the boxes are the first and third quartiles, and whiskers are the 2.5 and 97.5 percentiles (*i.e.* the boxplots cover the 95% confidence interval).

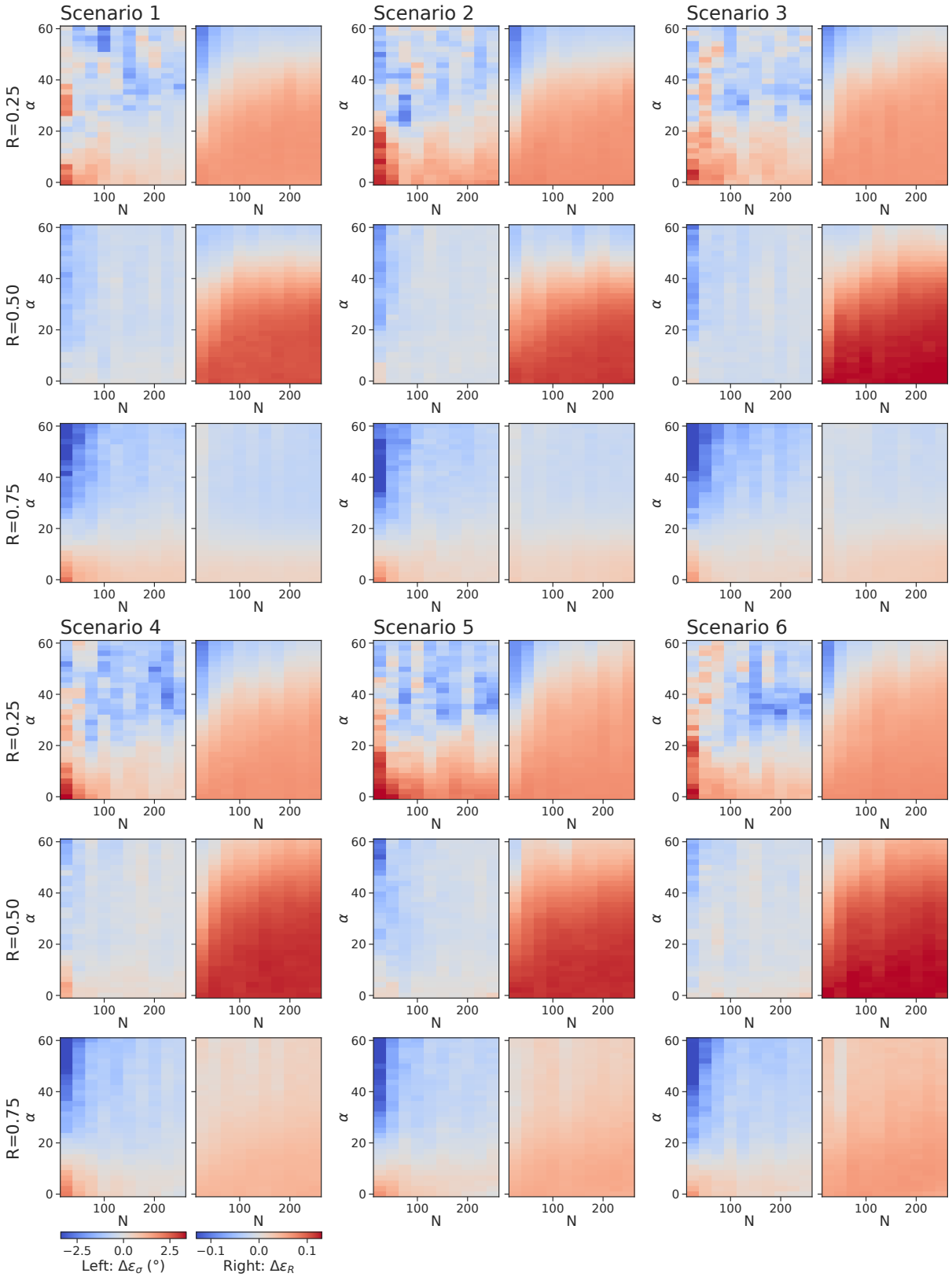

Figure S3: Error differences between the constant and the variable shear stress methods for every data scenario. The figure reads as a table where each 2-panel subfigure corresponds to a data scenario (column) and a shape ratio (row). See Table 1 in the main manuscript for the definitions of the data scenarios. Inside each subfigure, the left panel shows the error difference in stress orientations and the right panel shows the error difference in shape ratios, as a function of data set size (x-axis) and noise level (y-axis).

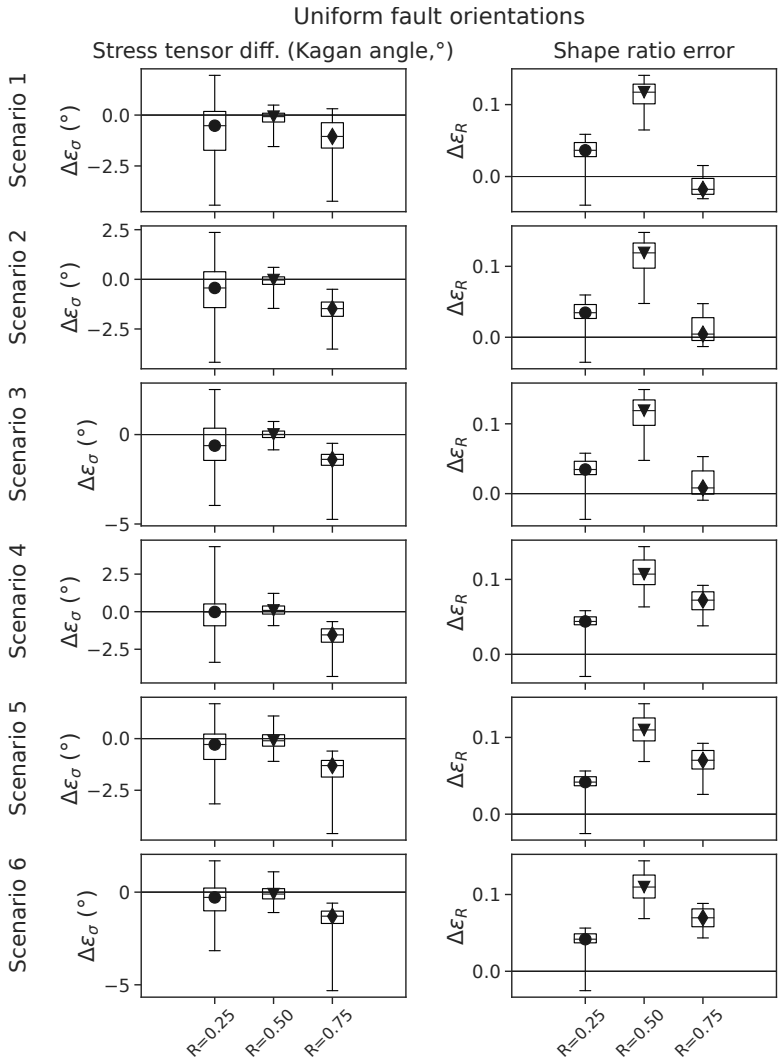

Figure S4: Summary of the error differences between the constant shear and variable shear methods with the uniform fault orientation sampling strategy (see Figure 2 in the main text). Each of the two columns shows the distribution of one relative error parameter ($\Delta\epsilon_\sigma$, $\Delta\epsilon_R$). Same legend as Figures S2.

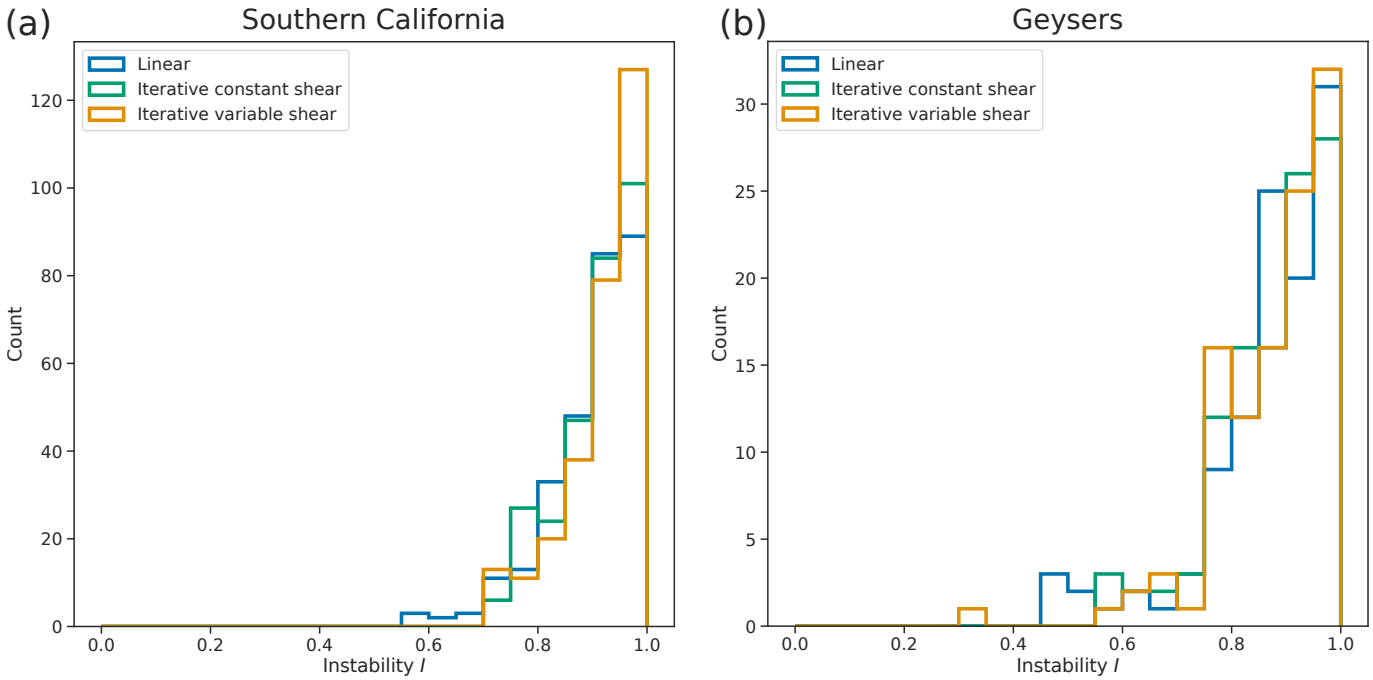

Figure S5: Instabilities estimated from the inverted stress tensors on **(a):** The Southern California data set, and **(b):** The Geysers data set.